Research Square

Preprints are preliminary reports that have not undergone peer review.
They should not be considered conclusive, used to inform clinical practice,
or referenced by the media as validated information.

Calibration and commissioning of 256-pixel SiPM Imaging Camera for 4-Meter Cherenkov Telescope

Bharat B. Singh

bbsingh@tifr.res.in

Tata Institute of Fundamental Research

Atreyee Sinha

Tata Institute of Fundamental Research

Abhradeep Roy

Tata Institute of Fundamental Research

N. K. Parmar

Tata Institute of Fundamental Research

M. Ranjan

Tata Institute of Fundamental Research

Sandeep Duhan

Tata Institute of Fundamental Research

B. K. Nagesh

Tata Institute of Fundamental Research

Kiran S. Gothe

Tata Institute of Fundamental Research

Shobha K. Rao

Tata Institute of Fundamental Research

S. S. Upadhya

Tata Institute of Fundamental Research

V. R. Chitnis

Tata Institute of Fundamental Research

Pratik Majumdar

Saha Institute of Nuclear Physics

Research Article

Keywords: SiPM, Cherenkov Telescope, VHE gamma rays, SPE spectrum

Posted Date: March 26th, 2026

DOI: https://doi.org/10.21203/rs.3.rs-9072158/v1

License: This work is licensed under a Creative Commons Attribution 4.0 International License.
Read Full License

Additional Declarations: No competing interests reported.

Calibration and commissioning of 256-pixel SiPM Imaging Camera for 4-Meter Cherenkov Telescope

Bharat B. Singh[a,*], Atreyee Sinha[a], Abhradeep Roy[a], N. K. Parmar[a], M. Ranjan[a], Sandeep Duhan[a], B. K. Nagesh[a], Kiran S. Gothe[a], Shobha K. Rao[a], S. S. Upadhya[a], V. R. Chitnis[a], Pratik Majumdar[b]

[a]*Depertment of High Energy Physics, Tata Institute of Fundamental Research, Dr Homi Bhabha Road, Colaba, Mumbai 400005, India*
[b]*Saha Institute of Nuclear Physics, 1/AF, Bidhannagar, Kolkata 700064, India*

Abstract

A 256-pixel Silicon Photomultiplier (SiPM) camera has been developed for a 4-meter diameter atmospheric Cherenkov telescope for ground-based gamma-ray astronomy at energies above 500 GeV. An accurate and stable camera performance requires regular, precise calibration of its readout chain. This paper presents the calibration methodology and results obtained using a dedicated calibration box developed in-house, employing a nanosecond pulsed light flasher operating at 405 nm, which provides a controlled and uniform illumination of the camera at few photoelectrons level. Absolute gain and photoelectron spectra were measured for each pixel under low-light conditions. Calibration measurements were initially performed on a laboratory test bench and subsequent repeated on site during telescope operations. The on-site calibration results show excellent agreement with the laboratory measurements, demonstrating the stability and robustness of the calibration procedure under actual observing conditions. The consistency between laboratory and in situ calibrations will allow the same calibration constants to be applied to both observational data analysis and detector simulations, thereby improving the accuracy of the instrument response and the reliability of the derived astrophysical measurements.

Keywords: SiPM, Cherenkov Telescope, VHE gamma rays, SPE spectrum

*Corresponding author: bbsingh@tifr.res.in

1. Introduction

A 256-pixel SiPM-based Imaging Camera has been developed at TIFR, Mumbai for ground based gamma ray astronomy at energies above 500 GeV. This camera was designed to be mounted on one of the Vertex elements of the the TACTIC telescope. The TeV Atmospheric Cherenkov Telescope with Imaging Camera (TACTIC), a compact array of four telescopes, was set up at Mount Abu (24.6° N, 72.7° E, 1300 m above sea level) in year 1997 by Astrophysical Science Division (APSD) of Bhabha Atomic Research Center (BARC). These telescopes are placed at the corners and center of an equilateral triangle of side 20 m. Single telescope at the center is being used as an imaging unit for indirect detection of the TeV gamma rays from celestial sources. One of the corner telescopes referred to as Vertex-2 (VE-2) was chosen for installation of the newly developed SiPM based imaging camera. The telescope reflector consists of 34 tessellated front coated mirrors of diameter 60 cm and focal length of $\approx$ 3.8 m. The light collector layout of the mirror facets follow a hybrid design, which is a parabolid near the optic-axis and Davis-Cotton in the periphery. The effective reflector area of the 4 m diameter dish is $\approx$ 9.5 m^2 and point spread function (PSF) of the light collector has diameter (D_{90}) of 0.34^o($\equiv$ 22.8 mm) Tickoo et al. [2005], Koul et al. [2007].

Each pixel comprises a HAMAMATSU-manufactured SiPM with a size of 13 mm $\times$ 13 mm. The camera provides a total field of view (FOV) of 5.0°, with an angular resolution of 0.33° per pixel. The camera has been designed with a modular architecture to simplify the troubleshooting of its various sub-systems. The front-end electronics are organized into Pixel Cluster Modules (PCMs), each serving 16 pixels. Every PCM includes light concentrators, SiPMs, preamplifiers, low voltage power supply board and a microcontroller-based bias supply system to maintain constant gain during operation. Details of the camera design have been previously published and more details may be found in Kumar et al. [2023b], Rao et al. [2023]. A dedicated low-voltage power supply (LVPS) board delivers regulated voltages of 3.3 V to each amplifier and +5 V to the bias supply modules. Hollow-type light concentrators with square entry and exit apertures are mounted in front of the SiPMs to improve light collection efficiency and suppress stray background light. Temperature sensors installed on the SiPM mount and bias boards, monitor the thermal fluctuations caused by the environment and electronic components. These sensors provide real-time feedback to the bias supply microcontrollers,

ensuring stable gain performance under varying temperature conditions.

The entire back-end readout electronics of the system is based on modular design and comprises 16 Cluster Digitizer Modules (CDMs), each handling 16 channels. Every CDM is equipped with four DRS-4-based Digitizer Boards (DDBs) Kumar et al. [2023a]. In addition, the readout system includes a Data Concentrator Module (DCM) and a Control & Trigger Module (CTM), all housed within a customised VME crate. Triggering is implemented in three levels: the first and second-level triggers are generated on the CDM motherboard, while the third-level trigger is formed on the CTM. This third-level trigger is matched against predefined geometric patterns, specifically the 3-NCNN (non collinear nearest neighbour) pattern, and is validated as the final trigger that initiates data acquisition. A 10 MHz system clock on the CTM, synchronized with a 1 Hz pulse from a Meinberg GPS unit, provides event time stamping with a timing precision of 100 ns. The system continuously monitors and records the count rate and anode current for each SiPM pixel. The DDB digitizes analog waveforms from SiPM-detected light flashes at a sampling rate of 1 GS/s. Front-end monitoring and control of the camera are managed by a Raspberry Pi based system. For data communication and transfer, the system uses a Wiznet W5300 TCP/IP hardware offload engine, which is managed by a NIOS soft-core processor and connected over an Ethernet link Duhan et al. [2026]. A Sky Quality Meter (SQM) Unihedron mounted on the back of the camera quantitatively monitors the brightness of the sky.

This work presents the design of a dedicated nanosecond light flasher developed for the characterization and calibration of SiPMs, both in laboratory (test bench) and in situ configurations. The light flasher is instrumental in evaluating the performance of light concentrators, optimizing the pixel-level readout chain, and validating the overall response of the camera camera system under real observational conditions.

2. Camera Calibration Box

Very high energy (VHE) gamma rays from celestial sources are indirectly detected using the ground based atmospheric Cherenkov telescopes Weekes [1988], Aharonian and Völk [1994], Hillas [1996]. Relativistic charged particles produced by gamma rays in the atmosphere induce polarization, leading to the emission of Cherenkov light. After undergoing absorption and scattering in the atmosphere, the Cherenkov photons peak at a wavelength of

around 350 nm and arrive as a brief flash lasting only a few nanoseconds. In order to calibrate the response of SiPMs to Cherenkov photons, a nanosecond light flasher, referred to as the Camera Calibration Box (CCB) was designed and developed at TIFR. The design incorporates concepts from prototype calibration systems developed previously Palatiello et al. [2017] and is fully compatible with SiPM-based photosensors. It illuminates the SiPM photo sensors and mimics Cherenkov photons. The CCB is being used for in situ calibration and continuous monitoring of camera pixels.

The calibration box is required to be a self-monitoring system capable of producing few nanoseconds light pulses, ranging from 1 photoelectron (pe) up to at least 1000 pe. A nanosecond pulse laser of 405 nm, Thorlabs NPL41B, is used as the light source, with a repetition rate of up to 10 MHz. The laser delivers optical pulse photons at minimum pulse width of 6 ns with an average energy of 1.5 nJ per pulse. A 12-stage motor-driven filter wheel (FW212CNEB), equipped with preloaded neutral density (ND) filters, is used to attenuate the intensity of light pulse produced by the laser source. A pair of ground glass diffusers (grit size 600) is used to scatter the laser beam, producing uniform illumination. The exit window, mounted at a right angle to the direction of the incident light source and coupled with the light diffuser assembly, provides uniform diverging illumination across the telescope's focal plane. A Raspberry Pi microcontroller, connected via an Ethernet link, is used for remote operation of the CCB.

Figure 1(a) shows the complete assembly of the CCB, including the light source (laser), optical diffuser, collimation optics, and mechanical housing. The laser source produces single, nanosecond-scale optical pulses when externally triggered with a 300 mV, 100 ns wide positive pulse. Figure 1(b) shows profile of the emitted light pulse, measured using a fast photomultiplier tube (PMT), demonstrates the generation of clean, nanosecond-scale pulses suitable for simulating Cherenkov light flashes. The optical pulse width of the laser source is set to 6 ns and remains preserved after multiple reflections within the light diffuser. The use of neutral-density filters reduces photon intensity, enabling the CCB to emit a low photon count. The photons produced by the CCB were analyzed using a Hamamatsu module (C11205), and the resulting photoelectron spectrum is shown in figure 1(c) and illustrate the ability of the CCB to produce discrete and stable light levels for gain calibration and single photoelectron resolution. Photoelectron measurements at different levels of optical density (OD) are presented in figure 1(d). These OD filters are factory calibrated and used to calibrate the CCB light system.

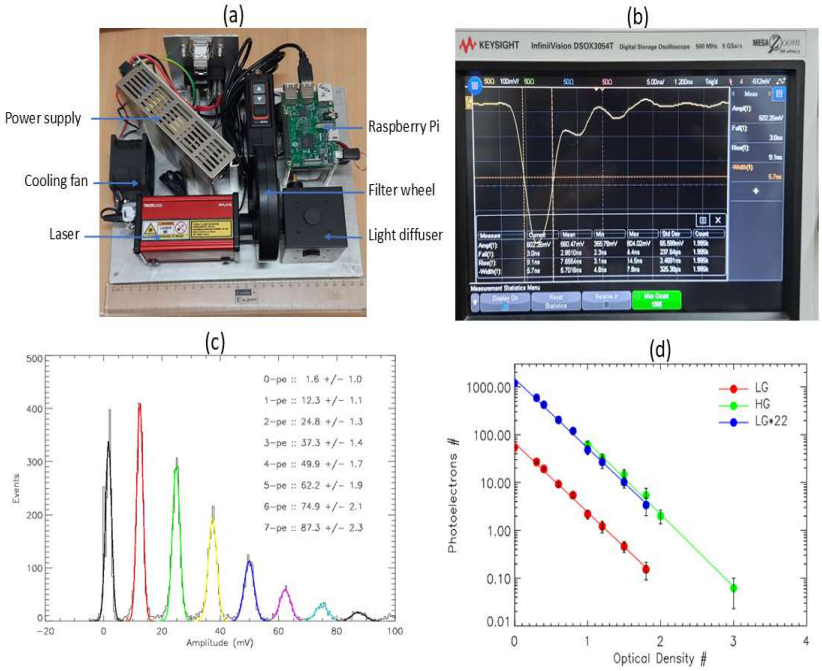


Figure 1: Design and performance of the Camera Calibration Box, (a) Assembled components of the light flasher system, (b) Characteristics of the light pulse measured using a fast photomultiplier tube, (c) Photoelectron spectrum recorded by a standard SiPM module under low light conditions and (d) Linearity response of the system across the full dynamic range.

To capture the complete dynamic range of photons produced by the CCB, a dual-gain amplifier with LG (low gain) and HG (high gain) settings was utilized. Using the pre-calibrated HG/LG ratio of 22, the full dynamic range of the CCB light system around 1000 photoelectrons was achieved. This also illustrates the linearity of light across its full dynamic range, indicating a proportional relationship between input light intensity and the output signal from the SiPM. These results validate the CCB's effectiveness for calibrating the pixel response over a wide range of photon fluxes. All measurements were conducted inside a light-tight black box at a baseline distance of 3.5 meters, corresponding to the distance between the telescope focal plane and the CCB.

3. Characterisation of Camera Components

3.1. SiPM

The camera employs a compact 4×4 channel Silicon Photomultiplier array (S13361-3050AS-04) HAMAMATSU, comprising 16 individual SiPMs, each with an active area of 3×3 mm^2 and a pixel pitch of 50 μm. The 3x3 mm^2 active area is divided into 3,584 cells/microchannels, giving high saturation threshold for photon counting. It exhibits low after-pulse characteristics and further provides reduced crosstalk and lower dark count. The device offers spectral sensitivity from 320 nm to 900 nm, with a peak detection efficiency of around 450 nm. The typical Photon Detection Efficiency (PDE) at this wavelength is approximately 40%. The temperature dependence of SiPMs is a critical factor that affects their gain, dark count rate, and overall performance stability. The SiPM gain is defined as the number of electrons generated per detected photon and can be expressed as

$$Gain(V,T) = \frac{C * (V_{bias} - V_{bd}(T))}{q} \tag{1}$$

where C is the microcell capacitance, V_{bias} is the applied voltage, V_{bd} is temperature-dependent breakdown voltage, and q is elementary charge. For normal operation of camera, it is essential to determine the breakdown voltage, its temperature dependence, and the absolute gain of individual SiPMs. This section provides an overview of these elements.

An SiPM is composed of numerous microscopic avalanche photodiodes (APDs) operating in Geiger mode. The breakdown voltage (V_{bd}) is a critical electrical parameter that marks the threshold at which each microcell enters avalanche operation. It is the minimum reverse bias voltage required for the electric field inside a microcell to become strong enough to initiate impact ionization, leading to a self-sustaining avalanche of charge carriers. Below V_{bd}, the device behaves like a conventional photodiode, without Geiger discharge, and produces very weak signal probably produced due to leakage current. When SiPM operated above V_{bd} (overvoltage, $V_o = V_{bias}$ - V_{bd}), each absorbed photon can trigger a complete avalanche, producing a large, well-defined, measurable pulse. In this work, the breakdown voltage of each SiPM was determined using the photoresponse method Chmill et al. [2017]. In this approach, the SiPM is illuminated with weak monochromatic light, and the pulse amplitudes are recorded as a function of the applied bias voltage.

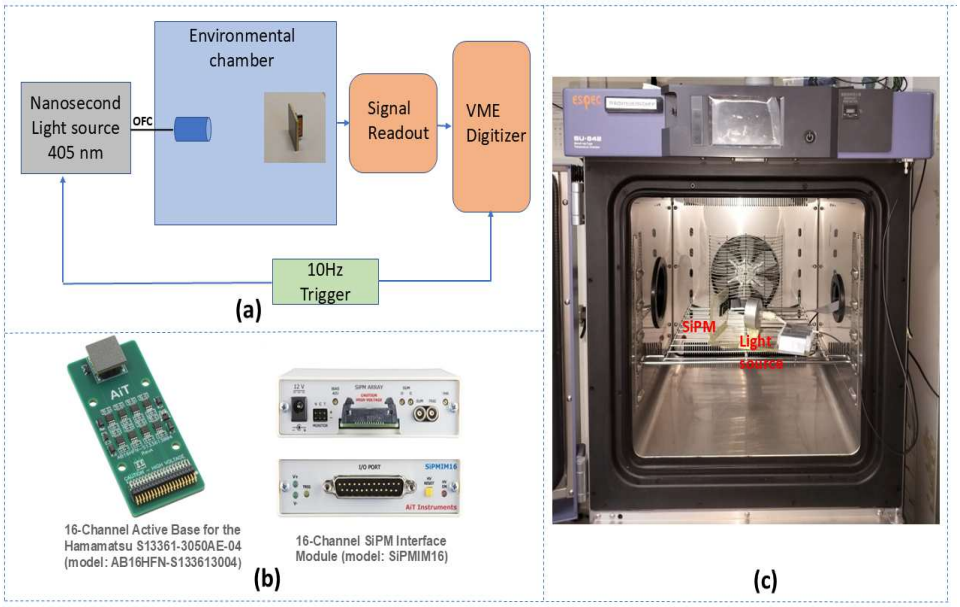


Figure 2: Measurement setup used for SiPM characterization. Panel (a) presents the block diagram, outlining the interconnections between the SiPM array, the readout electronics, the Camera Calibration Box (CCB), and the waveform digitizer. Panel (b) shows the readout circuits, including the 16-channel active base and signal-processing electronics used for channel-by-channel and summed-output acquisition. Panel (c) depicts the environmental chamber (ESPEC SU-642) used to house the SiPM during measurements, ensuring a light-tight and thermally controlled environment for stable operation.

Figure 2 shows the experimental setup used for SiPM characterization. A 16-channel active base (model: AB16HFN-S133613004, AiT Instruments) interfaced with a 16-channel controller (model: SiPMIM16) AIT-Instruments was used to read signals from Hamamatsu S13361-3050AS-04 series SiPMs. The readout system provides 16 buffered individual channel outputs, an analog sum output, and temperature monitoring. The SiPM, interfaced with the readout circuit, was housed inside a light-tight environmental chamber (ESPEC SU-642) to ensure stable operating conditions and prevent external light contamination. Illumination to SiPM was provided through an optical fiber, which was precisely aligned and coupled to the exit window of the CCB, enabling controlled delivery of light pulses to the SiPM. The analog outputs of each individual SiPM channel, along with the amplified summed signal, were routed to a VME-based waveform digitizer. The digitizer was configured with a sampling rate of 1 GS/s. The CCB was operated in a ex-

ternal trigger mode at a frequency of 10 Hz, generating light pulses at regular intervals. The pulse amplitude was recorded at operating bias settings incremented in 250 mV steps while maintaining a constant temperature. These measurements were repeated in a temperature range from -20°C to 30°C in 5°C steps. For each trigger, the complete waveform was captured and data was collected for a total of 5000 events.

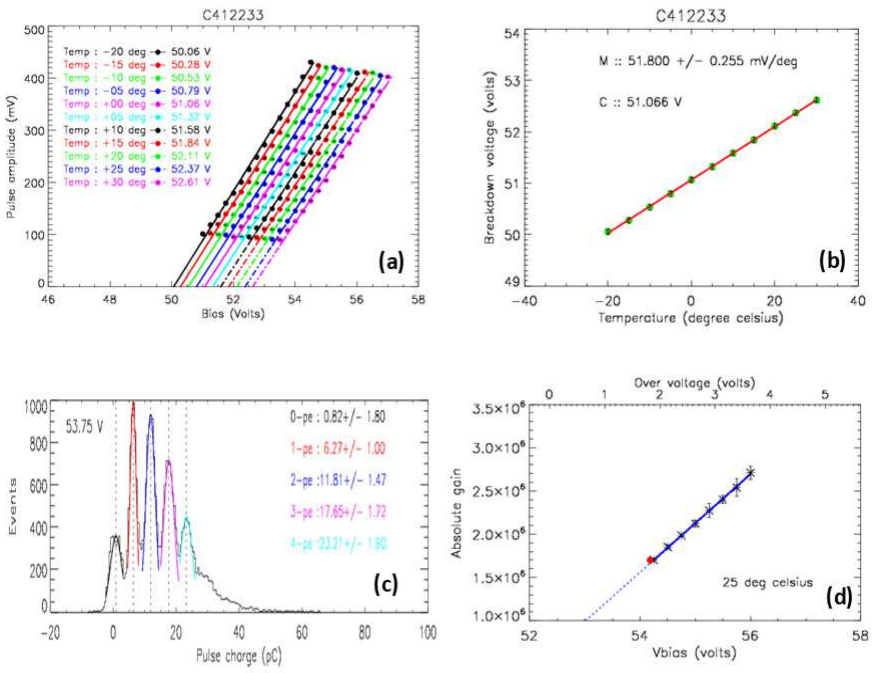


Figure 3: (a) Average pulse amplitude as a function of operating bias (size of error bar on mean is smaller than symbol size); (b) Breakdown voltage as a function of temperature; (c) Pulse charge distribution; and (d) Absolute gain as a function of operating bias and V_{ov}. The red data point represent value taken from the datasheet.

Figure 3 shows the results of the detailed characterization of a typical SiPM labeled C414233 used in the camera camera. Figure 3(a) illustrates the variation of the average pulse amplitude with the operating bias voltage, exhibiting a linear increase in signal strength. A linear fit was applied to the data obtained at a constant temperature, and the intersection of the fitted line with the x-axis provides the breakdown voltage. Figure 3(b) presents the

dependence of the breakdown voltage (V_{bd}) on temperature, revealing the characteristic linear increase in V_{bd} over the temperature range from $-20°C$ to $30°C$. The slope (M) of the fitted line represents the temperature coefficient, quantifying the rate at which the SiPM's breakdown voltage changes with temperature. The constant (C) corresponds to V_{bd} at $0°C$. Figure 3(c) displays the pulse charge distribution, where distinct peaks correspond to discrete photoelectron (p.e.) counts, enabling detailed signal and noise characterization. The average charge for each photoelectron peak was determined using Gaussian fits, and the single-photoelectron (SPE) charge was extracted from these averages. The absolute gain Dorosz et al. [2019] of the SiPM was calculated as:

$$\text{Gain}(V,T) = \frac{Q(V,T)}{f \times 1.6 \times 10^{-12}} \tag{2}$$

where Q is the SPE charge in picocoulombs, and f is the amplification factor of amplifier circuit. Figure 3(d) shows the variation of absolute gain with both operating bias and V_{ov}, demonstrating the expected linear increase in gain with V_{ov}. The measured results exhibit excellent agreement with the manufacturer's (Hamamatsu) datasheet values.

Figure 4 presents distributions of the key operational characteristics of the 256-pixel SiPM camera, highlighting both uniformity and pixel-to-pixel variations. Fig 4(a) shows the breakdown voltage distribution (V_{bd}) across all 256 SiPMs. Since individual pixels may exhibit slight differences in V_{bd}, the plot shows the spread of this fundamental parameter, which directly influences device operation. Fig 4(b) illustrates the distribution of the temperature coefficient of breakdown voltage, expressed in mV/°C. This parameter quantifies how sensitively each pixel's breakdown voltage shifts with temperature. Stable operation requires precise knowledge of this coefficient, as both V_{bd} and SiPM gain are temperature-dependent. In a small number of SiPMs, variations in manufacturing batches have caused deviations in breakdown voltage and temperature coefficients from the expected distribution. Panel (c) displays the spread of absolute gain values across the pixels, measured at a fixed overvoltage. This analysis helps evaluate how consistently different pixels amplify single-photon signals, which is crucial for uniform camera response. Finally, Panel (d) shows the distribution of overvoltage adjustments required for each pixel to achieve a constant target gain. This provides a measure of the correction needed to equalize performance across the camera, ensuring uniform signal amplification and reliable operation in real observations.

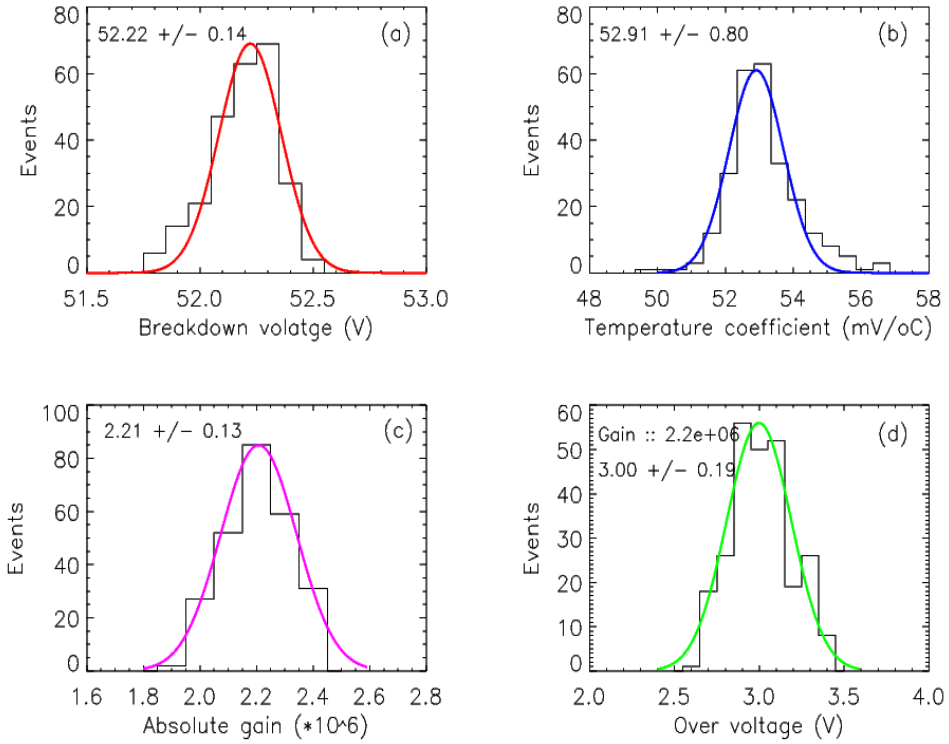


Figure 4: Distribution of measured parameters across all 256 pixels of camera:(a) Breakdown voltage, (b) Temperature coefficient, (c) Absolute gain at 3V overvoltage, and (d) Overvoltage required for constant gain operation.

4. Light Concentrator

The Compound Parabolic Concentrator (CPC), also known as a Winston Cone (WC)Welford and Winston [1989], is designed to collect and focus light from distant sources onto a detector smaller than the entrance aperture. Its acceptance angle is determined by the size of the entry/exit aperture and shape of parabolic profile. CPCs enhance light collection by allowing off-axis rays to undergo one or more reflections before exiting through the smaller aperture. Hollow-type CPCs have been implemented in a 256-pixel camera. The square-shaped entry and exit apertures of the CPC were chosen to optimize its efficiency. The light concentrators were fabricated from ABS plastic in two identical halves, each with a parabolic profile. Each half was first coated with aluminum, providing an average reflectivity of approximately 90% in the visible range, and then joined to form a single unit. A protec-

tive SiO_2 coating was applied to shield the reflective surface from weathering effects. Figure 5 presents the design, assembly, experimental setup,

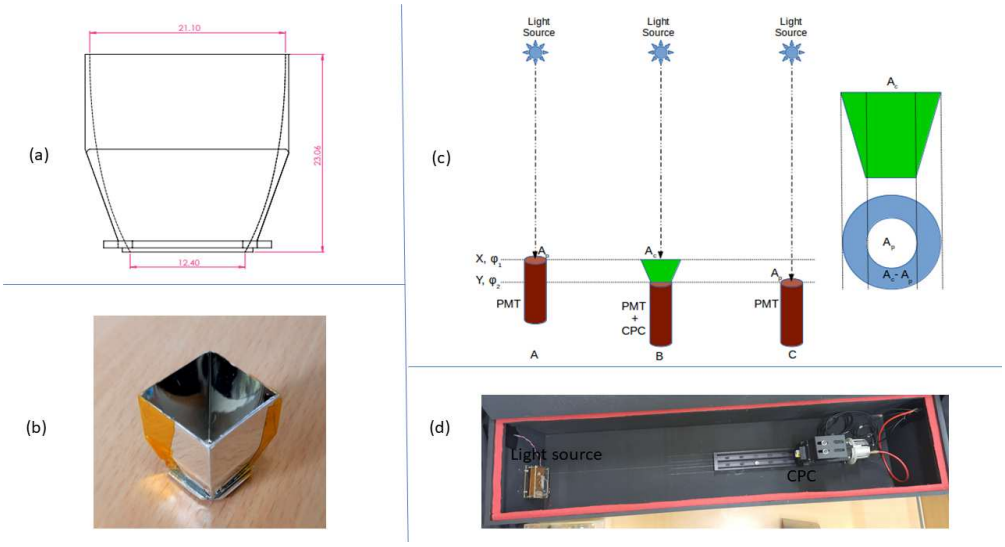


Figure 5: Design and Characterization of the CPC: (a) CAD model of the CPC, (b) Assembled CPC unit, (c) Methodology for measuring light collection efficiency, and (d) Experimental setup.

and methodology used in the characterization of CPC. Figure 5(a) shows the CAD model of the CPC, where both the entry and exit apertures are designed in a square shape to match the geometry of the SiPM. Figure 5(b) displays the photograph of the fully assembled CPC, formed by joining two identical halves into a single functional unit. Figure 5(c) illustrates the methodology used to evaluate the light collection efficiency (LCE) of the CPC. In this process, light is directed into the CPC, and the light flux is measured at both the entry (Position-X) and exit (Position-Y) apertures using a 50 mm diameter photomultiplier tube (PMT). Figure 5 (d) represents the actual experimental setup used for LCE measurements. It consists of a blue LED light source, motorized linear positioning stages (Zaber horizontal and vertical stages), and a PMT as the photodetector. A glass light diffuser was placed in front of the LED source to provide uniform illumination to the detector under test. The light concentrator was optically coupled to a PMT detector to evaluate its performance. The light collection efficiency of the CPC is calculated by using the following expression:

$$\eta = C * (\frac{I_B - I_C}{I_A}) \tag{3}$$

where I_A, I_B and I_C are measured photocurrent under different conditions A, B, and C, respectively. The constant C=0.59 is derived from the ratio of the entrance and exit aperture areas. For each CPC three measurements were carried out and the Average Light Collection Efficiency (ALCE) of more than 1300 CPCs was measured. A large fraction of the light concentrators that were tested exhibited light collection efficiencies below 70%, probably due to manufacturing defects or improper alignment during the joining of the two halves. Only 15% of the tested units demonstrated a light collection efficiency greater than 70%. Figure-6 shows the performance of CPCs, assembled CPCs on a predesigned mount plate in the form of a 4x4 array, and integrated with PCM. CPCs with an average LCE of more than 75% were selected for camera.

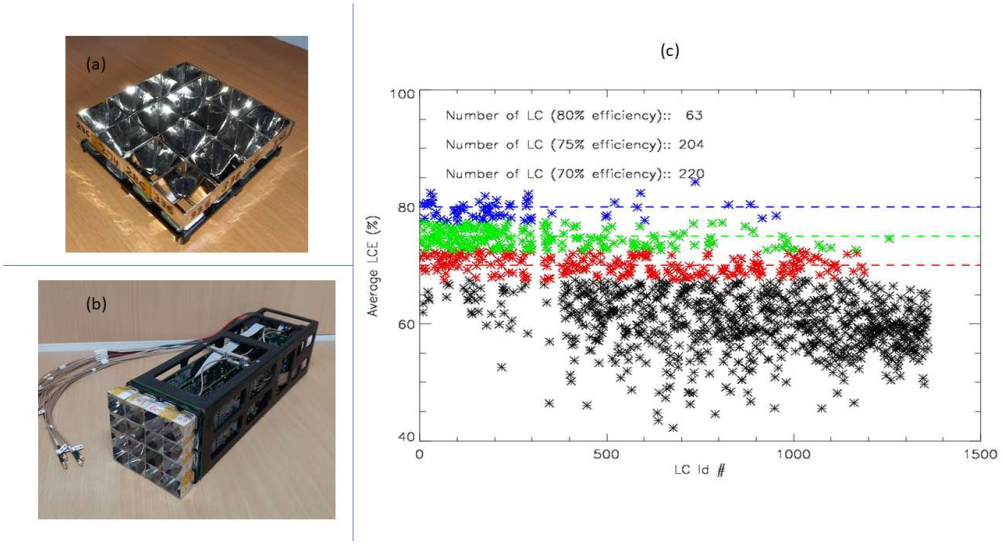


Figure 6: Characterization and Assembly of CPCs: (a) CPCs mounted on a predesigned plate in a 4×4 array, (b) Fully assembled Pixel Cluster Module (PCM), and (c) Average light collection performance of the CPCs.

5. In situ Measurements

The fully integrated camera is installed in the focal plane of the Vertex telescope (VE-2). High-speed fans mounted on the sides of the front and back-end sections provide air-based cooling. A quartz glass dichroic filter

blocks the bright night sky in the red region of the Cherenkov emission spectrum while allowing 92% transmission in the blue-visible (300 nm - 650 nm) range, thereby minimizing background light and protecting the photosensors from environmental dust, etc. The camera calibration box is positioned 3.5 meters from the focal plane and is integrated with both the network and the camera trigger system. Figure 7 highlights the position of the CCB and the front view of the camera with a dichroic glass filter. The following sub-sections detail the measurements conducted on-site for the photoelectron spectrum, the long-term monitoring plan of the camera pixels, and the optimal trigger thresholds for routine observation of cosmic-ray events.



Figure 7: The 256-pixel camera installed at the focal plane of the VE-2 telescope, highlighting: (a) Camera Calibration Box, and (b) the dichroic glass filter.

5.1. Photoelectron Spectrum

Accurate calibration of the camera photo-sensors is essential for reliable detection and reconstruction of cosmic-ray events. To achieve this, in situ gain measurements of the SiPMs were carried out under controlled low light conditions. The telescope dome was kept closed throughout the procedure to ensure a dark environment, effectively eliminating background light from natural sources such as moonlight and starlight, as well as from artificial lighting. This was critical to prevent any additional noise that could interfere with the detection of low-level signals and maintain the good accuracy

of the gain measurement. The CCB was configured with an optical density (OD) filter set to a value of 2.0, which significantly attenuated the emitted light. This ensured that only a small number of photons reached the camera, producing just a few photoelectrons per pixel, ideal for measuring gain in the low-light regime where single-photon sensitivity is required. During the calibration process, the waveform output from each pixel was recorded at a repetition rate of 50 Hz over 150 ns regions of interest (ROI). Over the course of the measurement, approximately 40,000 events were recorded which provide sufficient statistics to precisely determine the photoelectron spectrum of each individual SiPM pixel. A typical waveform recorded by the camera

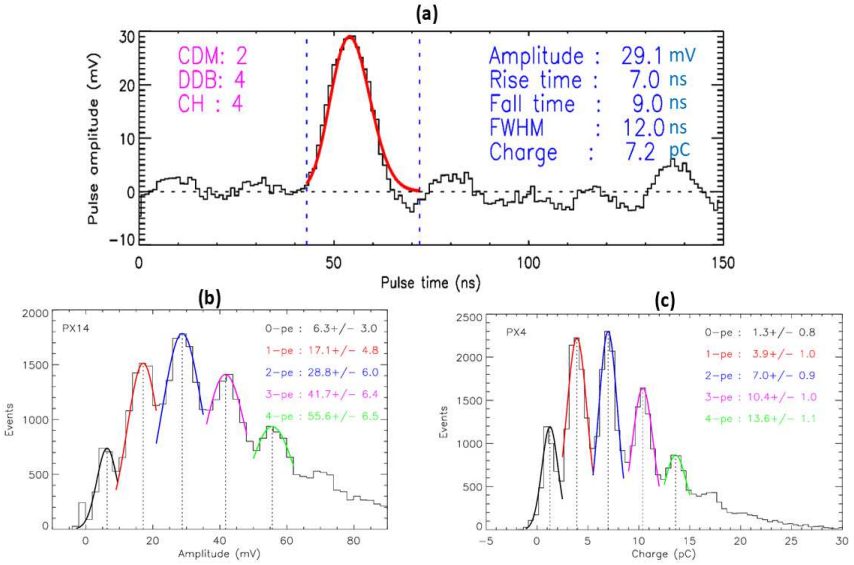


Figure 8: Response of SiPM pixel under low light illumination: (a) Typical pulse shape and with pulse parameters (b) Photoelectron spectrum measured in amplitude unit (c) Photoelectron spectrum measured in pico-coulomb unit.

digitizer under low illumination conditions is shown in Figure 8(a). This waveform corresponds to the response of a single pixel to a weak light pulse, typically resulting in only a few photoelectrons. To ensure accurate extraction of the signal characteristics, both the pre-pulse and post-pulse regions of the waveform are analyzed to establish and correct the baseline level. This baseline correction is essential for minimizing the impact of electronic noise and ensuring precise charge integration. A gamma function is then fitted to the waveform to model the pulse shape and extract relevant parameters such

as amplitude, rise time, fall time and pulse width. The start and stop times of the light pulse marked on the waveform and these boundaries define the integration window used to compute the total charge of the pulse. The charge is calculated by integrating the voltage over time and accounting for the 50Ω termination resistance of the digitizer input. Fig 8(b) and Fig 8(c) show the distributions of pulse amplitudes and pulse charges of a typical SiPM pixel. The first peak corresponds to the pedestal, representing events where no photons were detected by the SiPM. Each photoelectron (PE) peak was fitted with a Gaussian function, and the average single photoelectron (SPE) amplitude and charge were estimated from the differences between successive peaks. This measurement indicates that per pixel, on average, between 2 and 3 photoelectrons were detected. The pulse charge distribution exhibits a clearer separation of PE peaks compared to the pulse amplitude distribution.

Figure 9 presents in situ measurements of the SPE response, performed be-

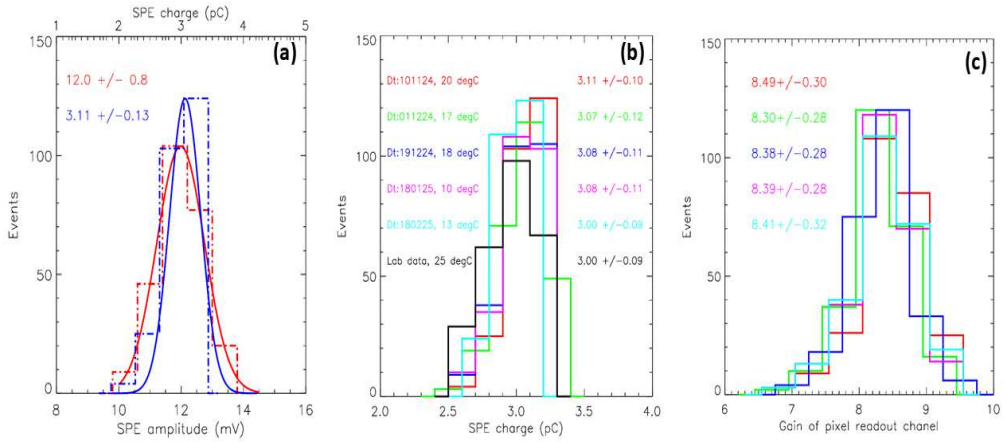


Figure 9: In situ measurement of the single photoelectron response of SiPM pixels: (a) Pulse amplitude and charge distributions, (b) Pulse charge distributions across five observation seasons, and (c) Gain distributions for pixel readout channels.

fore the start of each observation season. Figure 9(a) shows the distributions of the measured amplitude and charge of the SPE pulses. The average SPE pulse amplitude and charge are found to be 12.0±0.8 mV and 3.11±0.12 pC, respectively. These values can be used to convert any measured pulse amplitude or charge into photoelectron units. Figure 9(b) shows a comparative distribution of SPE pulse charges measured over five observation seasons.

These in situ measurements are in good agreement with the results obtained under laboratory conditions. Despite variations in ambient temperature up to approximately 15°C, the temperature-bias correction model, developed and validated in a controlled environment, was also found to perform effectively under field conditions. Figure 9(c) displays the gain distributions for individual pixel readout channels across the entire detector array. The average gain for the HG readout channels is determined to be 8.4±0.5, indicating a moderate spread in gain values and a reliable channel-to-channel calibration. Although a uniform response is maintained across the SiPMs, this indirect method of measuring pixel readout gain is still influenced by the photodetector response. These measured gain values are an essential input for detector simulations, where they are used to realistically model the electronic response of the system. In particular, they enable accurate reproduction of waveforms generated by incident Cherenkov photons, allowing precise pulse-charge integration in the data processing pipeline.

5.2. Operational Stability and Data Quality Monitoring

Periodic monitoring of the photosensors and associated front-end electronics of camera is essential to ensure consistent performance and high-quality data acquisition. This monitoring is carried out by uniformly illuminating the camera's pixels using a stable and calibrated light source. Data are recorded at regular intervals in dedicated calibration runs, referred to as FlashRuns, which are performed both before and after each science (source/background) observation run. During a FlashRun, a calibrated CCB, set to an optical density (OD) of 1.5, provides a uniform light pulse that delivers a sufficient number of photons to the camera pixels. The resulting signals are captured by both the HG and LG channels of the readout system, ensuring that the measurements remain within the dynamic range of the analog-to-digital converters (ADCs). Each FlashRun consists of 2,500 events recorded at a constant trigger rate of 50 Hz, providing statistically significant data to evaluate detector stability, gain consistency, and linearity over time. Figure 10(a) shows the pulse charge distributions recorded from the HG and LG channels of a representative pixel, derived from the waveform data. The ratio of the mean charge values from the HG and LG channels provides a gain conversion factor, which is used to normalize the LG data to the HG amplification scale, ensuring consistency across the two readout paths. Figure 10(b) presents the distribution of this HG/LG conversion factor across all 256 pixels of the camera. The relatively narrow spread of

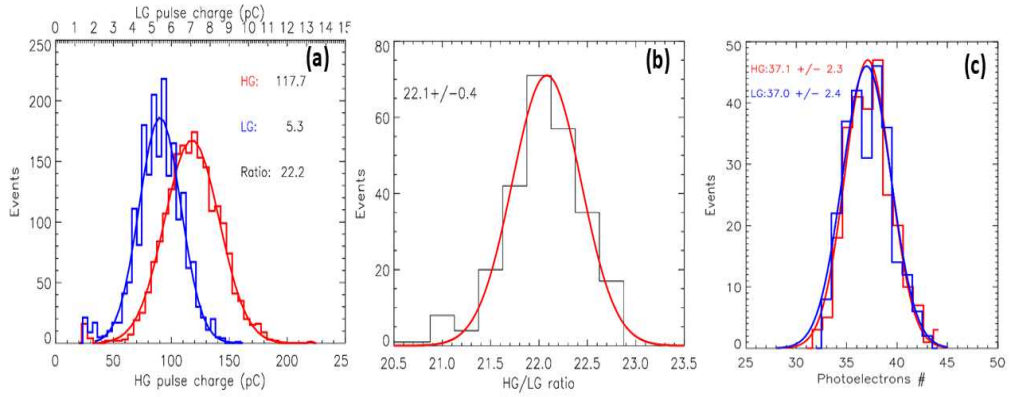


Figure 10: Pixel response from a typical FlashRun calibration Data: (a) Pulse charge distributions for the high-gain (HG) and low-gain (LG) channels, (b) Amplification factor between the HG and LG channels, and (c) Calibrated photoelectron measurements for both HG and LG channels.

values indicates a uniform response and consistent gain matching between HG and LG channels throughout the array. Finally, figure 10(c) displays the calibrated pulse charge data for both HG and LG channels, expressed in PE units. This calibration is performed using the previously determined HG/LG conversion factor along with the SPE charge value specific to each pixel. Figure 11 presents the two-dimensional uniformity map of the camera pixels (in units of PE), derived from a typical calibration run data performed immediately before and after each source observation. These calibration runs allow for monitoring the relative response of all 256 SiPM pixels under uniform illumination conditions. The map illustrates the spatial consistency of the pixel response throughout the focal plane. The consistent and uniform pixel behavior observed on such a map confirms the reliable performance of the camera system. Figure 12 shows a two-dimensional map of pulse arrival times measured relative to a standard TREF pulse Kumar et al. [2023a], Duhan et al. [2026]. The maximum spread in pulse arrival times is approximately 6 ns for both the HG and LG channels. The characteristic band structures observed in the arrival times arise from differences in propagation delays across the DDB and CDM motherboards.

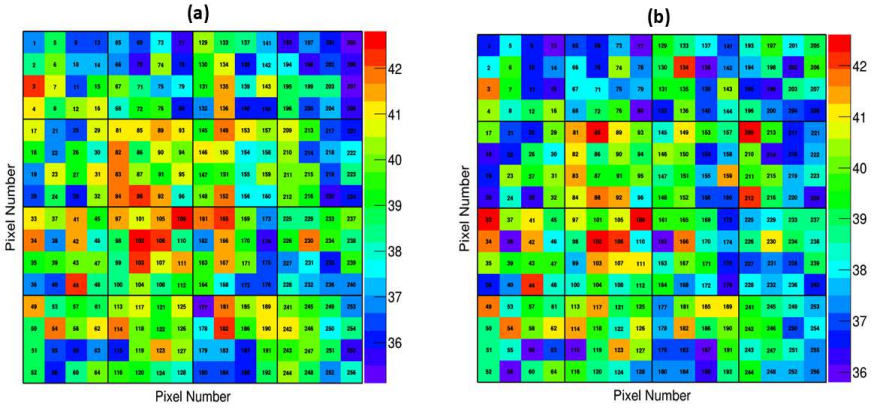


Figure 11: Pixel response uniformity maps showing gain stability and calibration consistency: (a) Before source run, (b) After source run.

5.3. Event Rate Optimization

On clear, moonless nights, the night sky background (NSB) limit the detection of Cherenkov photons produced by high-energy cosmic rays and gamma-ray interactions in the atmosphere. Although NSB photons arrive randomly in time, their high rate typically around 100 MHz can result in a considerable number of spurious triggers, leading to noise-contaminated data and increased dead time in the data acquisition system. Left panel in figure-13, the red, green and blue fields correspond to trigger FOV areas of 3.0°, 3.6°, and 4.2°, respectively. The progression from red to blue highlights the incremental expansion of the detection area, which is useful to evaluate the impact of different trigger FOV settings on system performance. Right panel in figure-13 illustrates the trigger rate as a function of the discriminator threshold (in mV), measured from a dark region of the sky under low zenith-angle conditions (below 15°). These measurements were carried out at a bias voltage of 3.2V overvoltage (OV) using the 3−NCNN trigger logic. The black-filled circles fitted with black dash-dotted lines indicate the contribution from SiPM dark counts and readout electronics noise. This component becomes negligible approximately above 5 PE, beyond which the effect of dark counts is suppressed due to the discriminator threshold. The steeply falling curve, fitted with a dot-dash line and extrapolated, is result of triggers dominated by the combined effect of NSB and residual SiPM dark counts. As the threshold increases, these background-induced triggers drop off rapidly. In contrast, the flat and more gradually declining curve, also

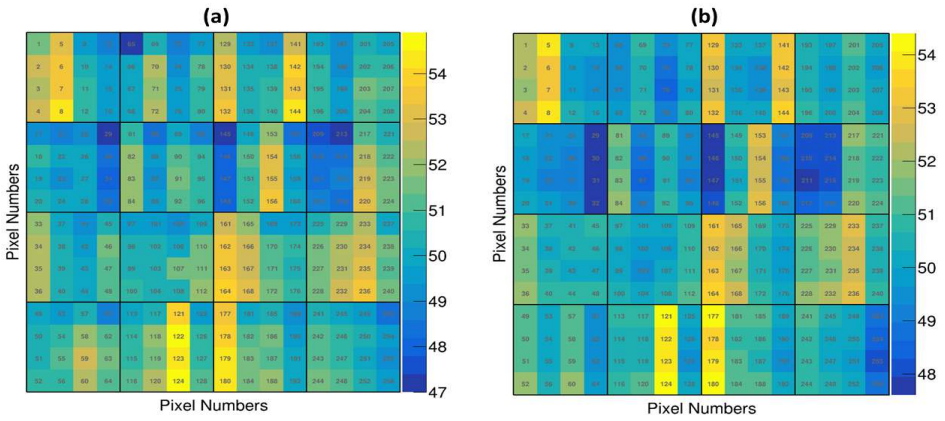


Figure 12: Pulse arrival time (ns) with respect TREF pulse: (a) HG channels, (b) LG channels.

fitted with a solid red, green and blue lines for trigger scheme A, B and C, corresponds to genuine Cherenkov events produced by cosmic-ray-induced air showers. These events dominate at higher thresholds where background noise due to NSB is effectively suppressed. At a discriminator threshold of 150 mV, the three trigger scheme typically records data at a rate of about 15.0±2.1 Hz,11.5±1.8 Hz and 7.0±1.0 Hz, respectively, and maintaining the accidental (chance) trigger rate below 1%.

Figure 14(a) shows the variation of the trigger rate as a function of OV, measured in steps of 250 mV under dark-sky conditions. These measurements help characterize the optimal operating range of SiPMs in terms of sensitivity and noise performance. At low OV, particularly below 1.5V OV (represented by the blue curve), the trigger rate remains low, typically a few Hz, due to the reduced gain and photon detection efficiency (PDE) of the SiPMs. In this regime, the SiPMs are less responsive to both signal and noise, resulting in minimal chance triggers. As the OV increases, the trigger rate gradually increases, reaching a moderate level at around 3V OV (indicated by the green curve). In this range, the SiPM gain and PDE are sufficiently high to efficiently detect Cherenkov photons while still maintaining a low rate of false triggers due to dark and NSB counts. This regime represents an operational "sweet spot," balancing sensitivity and noise suppression. However, beyond 3.75V OV, the trigger rate increases sharply (shown by the red

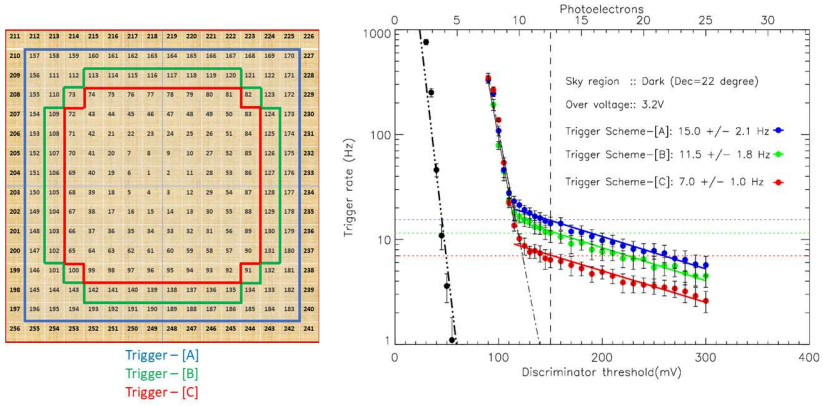


Figure 13: Performance of camera under dark sky condition: The left panel illustrates the trigger areas for cases A, B, and C. The right panel displays the corresponding rate-threshold measurements at 3.2V OV for each of these trigger areas.

curve), primarily due to the non-linear increase in dark count rate and correlated noise effects such as optical cross-talk and afterpulsing. The measured dark count rate of a typical SiPM pixel as a function of discriminator threshold is shown in Figure 14(b). The results indicate that the dark count rate exhibits an exponential dependence on the OV. These noise sources begin to dominate the trigger logic, leading to a higher rate of spurious events. These measurements confirm that the SiPMs can be operated within a flexible and well-defined optimal OV range, depending on observational conditions and scientific goals.

6. Conclusions

The camera for small size Imaging Atmospheric Cherenkov Telescope was specifically designed with the goal of long-term monitoring of blazars, highly variable astrophysical sources that provide critical insights into particle acceleration mechanisms during both flaring and quiescent states. One of the primary design challenges was selecting a suitable SiPM with a large photosensitive area to effectively capture the wide PSF characteristic of the optical system. After careful evaluation, the Hamamatsu S13361-3050-AS-04 SiPM, was selected to meet the requirements. The CPC design, with square entry and exit apertures, enabled moderate light collection efficiency while maintaining pixel-to-pixel isolation. This design will be upgraded to a hexagonal

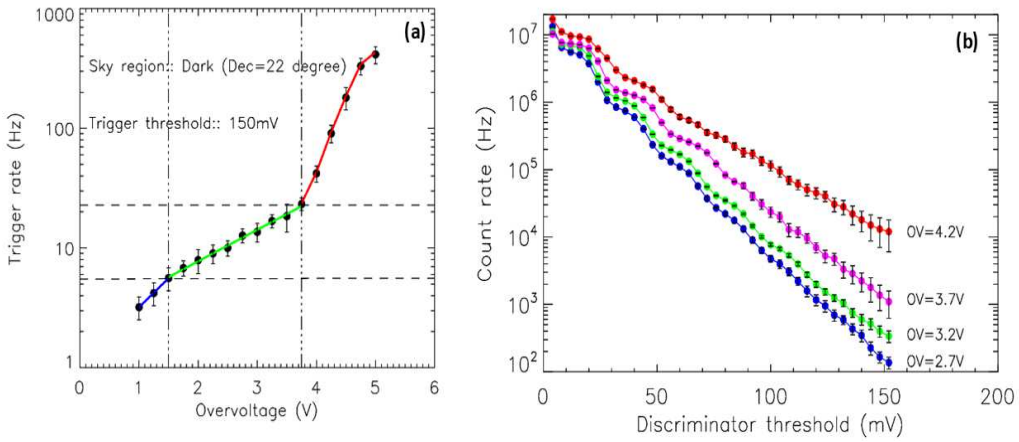


Figure 14: Optimization of standard operating bias: (a) Trigger rate vs over voltage , (b) The measured dark count rate vs discriminator threshold of a typical SiPM at 25 °C. For an OV of 3.2 V, the single-pixel dark count rate was found to be 338 ± 66 Hz at a discriminator threshold of 152 mV (corresponding to approximately a 13 PE trigger threshold).

CPC configuration in future iterations to further optimize the optical performance. A custom-designed, low-noise trans-impedance preamplifier was developed to linearly add the multi anode SiPM signal to a level equivalent to a single-anode response. Additionally, a low-cost nanosecond light pulse flasher was built, to match the characteristics of atmospheric Cherenkov photons. This flasher system has been used extensively in both laboratory and in-situ calibration routines. The comprehensive characterization of all 256 SiPMs in a controlled laboratory environment established a robust database of operational parameters across a wide temperature range. This data serves as a foundation for stable camera operation under varying environmental conditions. The successful validation of linear signal summation from sub-pixel channels, along with the implementation of a bias-voltage temperature compensation model, ensures high-accuracy signal processing in field conditions. In situ measurements of single photoelectron (SPE) charge and amplitude were used to establish a reliable conversion table, enabling the precise calibration of the data recorded by the digitizer modules of the camera. The HG channel is mainly used for trigger generation and pixel rate monitoring, with a dynamic range up to 80 photoelectrons. In contrast, the LG channel extends the measurable dynamic range up to 1500 photoelectrons Rao

et al. [2023], allowing for accurate reconstruction of high energy events. To reduce the impact of night-sky background, particularly in the near-infrared region where Cherenkov light contribution is minimal, a dichroic glass filter was integrated into the optical system. This filter effectively suppresses wavelengths beyond 650 nm, improving signal-to-noise ratio and enhancing overall camera performance under dark-sky conditions. The measurement of rate thresholds, a critical component of any cosmic-ray observation system enabled the optimization of the telescope-camera configuration for celestial source detection. Trigger rate measurements performed across various SiPM bias voltage settings allow fine-tuning of the system's sensitivity and photoelectron detection range, ensuring adaptability to different observation scenarios. Routine calibration procedures which are essential for maintaining the integrity and scientific reliability of the recorded data over long-term observation campaigns, are now well established. Simulations are currently in progress, and a comprehensive comparison between Monte Carlo predictions and experimental data will be the subject of an upcoming paper.

7. Acknowledgements

This project has been carried out with the support of the Department of Atomic Energy (DAE), Government of India. We sincerely thank all the team members who contributed to the design, integration, and successful installation of the camera camera system at the Mt. Abu observatory site. We would like to especially acknowledge Shri Ramdas Deshmukh and Ms. Varsha A. Nikam for their significant contributions to the laboratory test bench setup. The mechanical design and fabrication of the camera and associated infrastructure were successfully completed under the supervision of Shri Piyuesh Verma and Shri A. P. Kutty, with valuable assistance from Shri Santosh Chavan. We also extend our gratitude to Shri Nawang Dorji and Shri Phunchok Dorji, as well as members of the TACTIC team, for their support and technical guidance in the integration of the telescope optics and drive control system.

References

F. A. Aharonian and H. J. Völk. Very High Energy Gamma-Ray Astronomy with Groundbased Imaging Cherenkov Telescopes. In W. Wamsteker, Malcolm S. Longair, and Y. Kondo, editors, *Frontiers of Space and Ground-*

Based Astronomy, volume 187 of *Astrophysics and Space Science Library*, page 705, January 1994. doi: 10.1007/978-94-011-0794-5_118.

AIT-Instruments. URL https://www.ait-instruments.com/AB16HFN_S133613004_p/ab16hfns133613004.htm&ved=2ahUKEwjyhti3k-KPAxW8xDgGHd-MNQ8QFnoECCQQAQ&usg=AOvVaw05nkexNsyu9JgVvFZBjVjl.

V. Chmill, E. Garutti, R. Klanner, M. Nitschke, and J. Schwandt. Study of the breakdown voltage of SiPMs. *Nuclear Instruments and Methods in Physics Research A*, 845:56–59, February 2017. doi: 10.1016/j.nima.2016.04.047.

P. Dorosz, M. Baszczyk, W. Kucewicz, and L. Mik. Real-time measurement system with automatic gain detection and autocalibration for silicon photomultipliers. *Nuclear Instruments and Methods in Physics Research A*, 936:574–576, August 2019. doi: 10.1016/j.nima.2018.10.087.

Sandeep Duhan, Mano Ranjan, S. K. Rao, S. S. Upadhya, M. Saraf, N. K. Parmar, B. K. Nagesh, K. S. Gothe, B. B. Singh, Abhradeep Roy, N. Dorji, P. Dorjey, V. Chitnis, A. Sinha, K. Venugopal, K. Chanchalani, and S. Godiyal. Development of Control and Trigger Module for a 4-metre class imaging atmospheric Cherenkov telescope camera. *Nuclear Instruments and Methods in Physics Research A*, 1083:171074, March 2026. doi: 10.1016/j.nima.2025.171074.

HAMAMATSU. URL https://www.hamamatsu.com/content/dam/hamamatsu-photonics/sites/documents/99_SALES_LIBRARY/ssd/s13361-3050_eries_kapd1054e.pdf.

A. M. Hillas. Ground-based gamma-ray astronomy. *Nuovo Cimento C Geophysics Space Physics C*, 19C:701–712, October 1996. doi: 10.1007/BF02506663.

R. Koul, A. K. Tickoo, S. K. Kaul, S. R. Kaul, N. Kumar, K. K. Yadav, N. Bhatt, K. Venugopal, H. C. Goyal, M. Kothari, P. Chandra, R. C. Rannot, V. K. Dhar, M. K. Koul, R. K. Kaul, S. Kotwal, K. Chanchalani, S. Thoudam, N. Chouhan, M. Sharma, S. Bhattacharyya, and S. Sahayanathan. The TACTIC atmospheric Cherenkov imaging telescope.

Nuclear Instruments and Methods in Physics Research A, 578(3):548–564, August 2007. doi: 10.1016/j.nima.2007.06.011.

Sandeep Kumar, S.S. Upadhya, K.S. Gothe, N.K. Parmar, M. Ranjan, S.K. Rao, B.K. Nagesh, B.B. Singh, V. Chitnis, B.S. Acharya, and V. Bhatnagar. Development of a prototype 16-channel dual gain waveform readout and data transfer system for iact based telescope camera. *Nuclear Instruments and Methods in Physics Research Section A: Accelerators, Spectrometers, Detectors and Associated Equipment*, 1049: 168091, 2023a. ISSN 0168-9002. doi: https://doi.org/10.1016/j.nima.2023.168091. URL https://www.sciencedirect.com/science/article/pii/S0168900223000815.

Sandeep Kumar, S.S. Upadhya, N.K. Parmar, M. Ranjan, B.K. Nagesh, K.S. Gothe, B.B. Singh, S.K. Rao, V. Chitnis, B.S. Acharya, and V. Bhatnagar. A 16-channel programmable sipm bias supply system for cherenkov telescope imaging camera. *Journal of Instrumentation*, 18(01):T01005, jan 2023b. doi: 10.1088/1748-0221/18/01/T01005. URL https://dx.doi.org/10.1088/1748-0221/18/01/T01005.

M. Palatiello, D. Cauz, F. Ferrarotto, F. D. Persio, G. Pauletta, M. Iori, P. Majumdar, A. Chatterjee, V. Chitnis, B. B. Singh, K. Gothe, M. Manoranjan, and CTA Consortium. Test results of a prototype device to calibrate the Large Size Telescope camera proposed for the Cherenkov Telescope Array. In *35th International Cosmic Ray Conference (ICRC2017)*, volume 301 of *International Cosmic Ray Conference*, page 857, July 2017. doi: 10.22323/1.301.0857.

Shobha K. Rao, K.S. Gothe, S.S. Upadhya, N.K. Parmar, R.L. Deshmukh, B.B. Singh, Sandeep Kumar, M. Ranjan, A. Sarkar, S.R. Patel, and V.R. Chitnis. Analog signal processing for large area sipm in cherenkov telescope camera. *Nuclear Instruments and Methods in Physics Research Section A: Accelerators, Spectrometers, Detectors and Associated Equipment*, 1051: 168191, 2023. ISSN 0168-9002. doi: https://doi.org/10.1016/j.nima.2023.168191. URL https://www.sciencedirect.com/science/article/pii/S016890022300181X.

A. K. Tickoo, R. L. Suthar, R. Koul, M. L. Sapru, N. Kumar, C. L. Kaul, K. K. Yadav, S. Thoudam, S. K. Kaul, K. Venugopal, M. Kothari, H. C.

589 Goyal, P. Chandra, V. K. Dhar, R. C. Rannot, M. K. Koul, and S. R. Kaul.
590 A generalized ray-tracing procedure for an atmospheric Cherenkov imaging
591 telescope and optical characteristics of the TACTIC light collector. *Nuclear*
592 *Instruments and Methods in Physics Research A*, 539:177–190, February
593 2005. doi: 10.1016/j.nima.2004.09.035.

594 Unihedron. URL https://www.unihedron.com/projects/sqm-le/.

595 Trevor C. Weekes. Very high energy gamma-ray astronomy. *Physics*
596 *Reports*, 160(1):1–121, 1988. ISSN 0370-1573. doi: https://doi.org/
597 10.1016/0370-1573(88)90177-9. URL https://www.sciencedirect.com/
598 science/article/pii/0370157388901779.

599 W. T. Welford and R. Winston. *High collection nonimaging optics*. 1989.